A flow-rate-aware data-driven model of vanadium redox flow battery based on gated recurrent unit neural network

Journal of Energy Storage 74 (2023) 109537

Contents lists available at ScienceDirect

Journal of Energy Storage

journal homepage: www.elsevier.com/locate/est

Research papers

A flow-rate-aware data-driven model of vanadium redox flow battery based on gated recurrent unit neural network

Binyu Xiong [a], Jinrui Tang [a], Yang Li [b,*], Peng Zhou [a], Shaofeng Zhang [a], Xinan Zhang [c], Chaoyu Dong [d], Hoay Beng Gooi [e]

[a] School of Automation, Wuhan University of Technology, Wuhan, China
[b] Department of Electrical Engineering, Chalmers University of Technology, Gothenburg, Sweden
[c] School of Electrical, Electronic and Computer Engineering, The University of Western Australia, Perth, Australia
[d] Agency for Science, Technology and Research, Singapore
[e] School of Electrical and Electronic Engineering, Nanyang Technological University, Singapore

ARTICLE INFO

Keywords:
Data-driven model
Flow rate
Gated recurrent unit
Neural network
Energy storage
Vanadium redox flow battery

ABSTRACT

The vanadium redox flow battery (VRB) system involves complex multi-physical and multi-timescale interactions, where the electrolyte flow rate plays a pivotal role in both static and dynamic performance. Traditionally, fixed flow rates have been employed for operational convenience. However, in today's highly dynamic energy market environment, adjusting flow rates based on operating conditions can provide significant advantages for improving VRB energy conversion efficiency and cost-effectiveness. Unfortunately, incorporating the electrolyte flow rate into conventional multi-physical models is overly complex for VRB management and control systems, as real-time operations demand low-computational and low-complexity models for onboard functionalities. This paper introduces a novel data-driven approach that integrates flow rates into VRB modeling, enhancing data processing capabilities and prediction accuracy of VRB behaviors. The proposed model adopts a gated recurrent unit (GRU) neural network as its fundamental framework, exhibiting exceptional proficiency in capturing VRB's nonlinear voltage segments. The GRU network structure is carefully designed to optimize the predictive ability of the model, with flow rate considered as a crucial input parameter to account for its influence on VRB behavior. Model refinement involves analyzing well-designed simulation results obtained during VRB operations under various flow rates. Laboratory experiments were also designed and conducted, covering different conditions of currents and flow rates to validate the proposed data-driven modeling method. Comparative analyses were performed against several state-of-the-art algorithms, including equivalent circuit models and other data-driven models, demonstrating the superiority of the proposed GRU-based VRB model considering flow rates. Thanks to the GRU's outstanding capability in processing time series data, the proposed model delivers impressively accurate terminal voltage predictions with a low error margin of no more than 0.023 V (1.3%) under wide operating ranges. These results indicate the efficacy and robustness of the proposed approach, highlighting the novelty and significance of accounting for flow rates in accurate VRB modeling for management and control system design.

1. Introduction

As an emerging energy storage technology, vanadium redox flow batteries (VRBs) offer high safety, flexible design, and zero-emission levels, rendering them particularly well-suited for long-duration operations and a promising option in our efforts to achieve future carbon neutrality [1–3]. Therefore, VRBs have demonstrated their potential in various modern applications, such as serving as reliable power sources for communication base stations, utility-scale energy storage, and microgrids [4,5]. As the scope of the applications widens, there is a growing need for highly precise VRB models for effective management of these delicate electrochemical devices. However, due to VRBs' complex operational mechanisms and the infinite-order nature, developing a simplified yet accurate VRB model for online use of advanced battery management and optimal control poses a fundamental challenge [6,7].

* Corresponding author.
E-mail addresses: bxiong2@whut.edu.cn (B. Xiong), yangli@ieee.org (Y. Li).

https://doi.org/10.1016/j.est.2023.109537
Received 29 July 2023; Received in revised form 4 October 2023; Accepted 31 October 2023
Available online 7 November 2023

Nomenclature

Abbreviation

BPNN	Back-propagation neural network
CNN	Convolutional neural network
DDM	Data-driven model
ECM	Equivalent circuit model
EM	Electrochemical model
GRU	Gated recurrent unit
Li-ion	Lithium-ion
LSTM	Long-short-term memory
MAE	Mean absolute error
MSE	Mean squared error
PSO	Particle swarm optimization
R^2	R-square
RMSE	Root-mean-square error
RNN	Recurrent neural network
SOC	State of charge
VRB	Vanadium redox flow battery

Symbol

α	Learning rate
$\bar{x}$	Normalized input of GRU or model
$\bar{y}$	Mean value of model output
β_1, β_2	Dynamic average rates
$\hat{G}$	Corrected G
$\hat{M}$	Corrected M
$\hat{y}$	Predicted value of model output
$\mathcal{L}$	Loss function
θ	All the learnable parameters
$\tilde{h}$	Candidate state of GRU
ϵ	Update parameter
b	A learnable parameter vector
f	GRU function
G	Second moment of g
g	Updated gradient
h	Output of GRU
M	First moment of g
n	Number of data samples
Q_{acc}	Accumulated charge
$Q_{\text{nom,chg}}$	Nominal charging capacity
$Q_{\text{nom,dch}}$	Nominal discharging capacity
r	Reset gate of GRU
U	A learnable parameter matrix
W	A learnable parameter matrix
x	Input of GRU or VRB model
$x_{\max}$	Maximum value of input data
$x_{\min}$	Minimum value of input data
y	Actual value of model output
z	Update gate of GRU
SOC_0	Initial SOC
SOC_{chg}	SOC during charging
SOC_{dch}	SOC during discharging

Subscript

i	Data sample index
j	$\in \{h, z, r\}$
t	Time index

Existing VRB models can be categorized into electrochemical models (EMs), equivalent circuit models (ECMs), and data-driven models (DDMs) [8]. EMs typically consist of a set of highly complex partial differential–algebraic equations, primarily used for battery design and performance analysis [9]. Developing a reliable EM requires in-depth knowledge of the internal mechanisms of VRBs, which can be a significant challenge for many power engineers who lack a background in electrochemistry and multi-physics modeling [10]. In contrast to EMs, ECMs are established to mimic the external characteristics through electrical equivalence [11]. Commonly used ECMs are based on the relationship among various electrical circuit components, such as resistance and capacitance [12]. ECMs often neglect the influence of the electrolyte flow rates on the VRB's external characteristics since the flow rate is typically considered fixed and not subject to adjustment during operation [13].

Recent studies, however, have revealed that varying the flow rates of VRBs might significantly improve their system efficiency [14,15]. For example, Khazael et al. conducted an analysis on how the flow rates affect VRB performance and found a correlation between flow rates and voltage drop [16]. This connection arises because the flow rate is closely related to the concentrations of vanadium ions and protons inside the battery, thus affecting the terminal voltage of VRBs [17]. By ignoring the influence of the flow rate, the terminal voltage is calculated based on a simple transformation and superposition of linear and negative exponential functions, limiting the fitting ability of nonlinear segments. Previous studies on the flow rate influence on the VRB mainly focused on establishing equivalent hydraulic models without considering the internal electrochemical characteristics. However, it is well-known that the hydraulic and electric fields in VRBs are highly coupled. A single equivalent circuit in the coupled model can only describe phenomenological behaviors within a limited operating range, while accurately replicating system behaviors and reflecting the completing internal operational mechanisms under all allowable operating conditions might require complex model structures and carefully designed experiments for identifying the high-dimensional model parameters [18,19].

In contrast, establishing a DDM does not require prior knowledge of system mechanisms or physical model structures, and the model accuracy can be readily improved by increasing the training data size and type [20]. Additionally, DDMs have outstanding capability to identify nonlinear characteristics, making them highly suitable for the diverse operating conditions of modern energy systems such as lithium-ion (Li-ion) batteries. For instance, in [21], Li-ion batteries were modeled using the back-propagation neural network (BPNN), and the BPNN's weights and thresholds were optimized using the particle swarm optimization (PSO) algorithm based on the Levy flight strategy. Another BPNN was proposed in [22], which was trained by the Levenberg–Marquardt algorithm and optimized through the genetic algorithm and PSO. However, in BPNNs, information is transferred in a unidirectional manner, and the influence of the past output on the present input is ignored, weakening the model's predictability. To address this problem, a multi-layer perceptron was employed to establish a Li-ion battery model in [23], where the data sequence was split into discrete points. Although the external characteristics of the battery show regularity and continuity over time, the models [20–24] ignored the time-series feature, resulting in limited accuracy for long-term data.

Due to the rapid growth in battery data volume in recent years, deep learning has been explored for modeling Li-ion battery to consider the features in the time series. For example, in [25], a Li-ion battery model based on a recurrent neural network (RNN) with a time lag was proposed. RNNs have a memory function that makes them suitable for simulating temporal processes. However, RNNs are limited in their ability to capture long-term dependencies in data, often leading to the issues such as gradient disappearance or explosion. To solve this problem, an RNN model in [26] divided the hidden layers into different modules by clock-controlled RNN and assigned specified

clock speeds for each module to mitigate the long-term dependencies. Nevertheless, traditional RNNs may still encounter gradient-related issues. Introducing a long-short-term memory (LSTM) unit can effectively control the information accumulation rate, selectively incorporate new information, and forget previous information, making them suitable for handling long-term series data. Thus, in [27,28], a convolutional neural network (CNN) and an LSTM network were combined and optimized by a honey badger algorithm. The gated recurrent unit (GRU) neural network is another option for long-term series data, offering memory capability similar to LSTM but with a simplified network structure and fewer hidden layer neurons. With their looped network knot, GRUs are more suitable for processing temporal data, thereby effectively improving the problem of long-term dependence [29]. A Li-ion battery model, featuring the GRU as its core component and employing deep feature selection was proposed in [30], where the input quantities were weighted before fed into the GRU structures.

While extending the aforementioned DDMs to VRB systems may seem straightforward, there remains a scarcity of relevant research in this domain. Assessing the applicability of existing data-driven techniques to VRBs requires individual evaluation, taking into account the notable structural and operational differences between Li-ion batteries and VRBs, as discussed earlier [31]. For example, pioneering studies on VRB DDMs based on deep learning were introduced in [20,28]. However, it should be noted that both of these studies assume a constant flow rate. Furthermore, in [29], a physics-informed CoKriging model was proposed, where the battery is discharged and charged at a constant current. These assumptions significantly deviate from the evolving requirements of new VRB applications, which demand continuous adjustment of flow rates [32].

In view of the above, this paper contributes to proposing a novel data-driven modeling framework tailored for VRBs, marking the early attempt of a flow-rate-aware approach. More specifically, we employ a GRU neural network to characterize VRB performance without the need for prior knowledge of the complex internal mechanisms. The GRU has the capability to approach the nonlinear characteristic of the VRB, and its recurrent and gated structures can alleviate the timing dependence problems of conventional neural networks to handle larger datasets. Flow rate, current, state of charge (SOC), and historical voltage are selected as inputs to the model, which reflects the VRB behaviors via multi-physics fields. Experiments under systematically varying current and flow rates are designed and conducted on a laboratory VRB platform to validate the proposed models.

The rest of this paper is organized as follows: Section 2 outlines the framework of the DDM of VRB, including the extraction of GRU-based temporal features and the setting of hyperparameters. Section 3 details the experimental platform, experimental design, and the data processing procedures. The effect of flow rates on the performance of VRBs is also analyzed. Section 4 assesses the accuracy of the proposed model under varying flow rates by comparing it with experimental data and other existing models. Finally, we present our concluding remarks are in Section 5.

2. A data-driven VRB model based on GRU neural networks

The flow-rate-aware DDM framework for VRBs is depicted in Fig. 1, consisting of three key steps:

(1) Determination of the model structure.
(2) Experimental design and data collection.
(3) Model training and validation.

To predict the VRB terminal voltage, the data sequences are first normalized and directed to the input layer. Subsequently, the temporal features of each sequence are individually extracted through a GRU layer. Given that the cutoff voltage of experiments is manually set, the sequences need to pass through a sigmoid layer to restrict the output within the range of [0,1]. Finally, a fully connected layer is utilized to calculate the model output.

Table 1
Hyperparameters of the GRU neural network.

Layer	Number of neurons	Activation function
Input Layer	4	–
GRU Layer	64	State activation function: tanh Gate activation function: sigmoid
Sigmoid Layer	64	Sigmoid
Fully-Connected Layer	1	–
Output Layer	1	Loss function: MSE

2.1. Temporal feature extraction based on GRU

Since the external characteristics of VRBs exhibit regularity and continuity over time, continuous data in time contain more information [33]. Therefore, the time-series model of VRB based on neural networks can approximate nonlinear relationships and better handle the connections between external characteristics. The GRU-RNN is shown in Fig. 2, where we use the subscripts t and $t-1$ to represent the current and the previous time instants, respectively, and x_t and h_t represent the input and the output of the GRU, respectively. Since the GRU has fewer parameters than the LSTM, the training process of the GRU is more straightforward and faster [29,33]. The GRU state is updated by:

$$h_t = z_t \odot h_{t-1} + \left(1 - z_t\right) \odot \tilde{h}_t \tag{1}$$

$$z_t = \sigma\left(W_z x_t + U_z h_{t-1} + b_z\right) \tag{2}$$

$$\tilde{h}_t = \tanh\left(W_h x_t + U_h\left(r_t \odot h_{t-1}\right) + b_h\right) \tag{3}$$

$$r_t = \sigma\left(W_r x_t + U_r h_{t-1} + b_r\right) \tag{4}$$

where $\odot$ represents the element-wise product. $\tilde{h}_t$, z_t, and r_t are the candidate state, the update gate, and the reset gate, respectively. The update gate $z_t \in [0,1]$ is used to balance between the input and forget and the reset gate $r_t \in [0,1]$ is to control the dependence of the candidate state on the previous state. Furthermore, W_j, U_j, and b_j ($j \in \{h,z,r\}$) represent the learnable network parameters associated with the specific network structure.

2.2. Selection of hyperparameters

The selection of model hyperparameters is accomplished through an iterative trial-and-error approach. Specifically, the batch size is set to 16, the learning rate is set to 0.005, and the model employs a single-layer GRU structure. The numbers of neurons in the input and output layers are determined by the numbers of input and output features. The hyperparameters of the GRU neural network used in this work are given in Table 1.

2.3. Training the GRU neural network

This subsection provides a concise overview of the GRU neural network training process. Initially, the data undergo normalization to eliminate the influence of different scales and units as follows:

$$\bar{x}_i = \frac{x_i - x_{\min}}{x_{\max} - x_{\min}} \tag{5}$$

where $x_{\max}$ and $x_{\min}$ are the maximum and the minimum values in the dataset, respectively. Normalizing the data ensures that the neural network effectively processes and learns from the input features without being skewed by variations in scales or units, leading to more accurate and reliable predictions. Subsequently, we employed the mean squared error (MSE) as the chosen loss function for the training process.

$$\mathcal{L}\left(\hat{y}_i, y_i\right) = \frac{1}{n}\sum_{i=1}^{n}\left(\hat{y}_i - y_i\right)^2 = \frac{1}{n}\sum_{i=1}^{n}\left(f\left(\bar{x}_i, \theta\right) - y_i\right)^2 \tag{6}$$

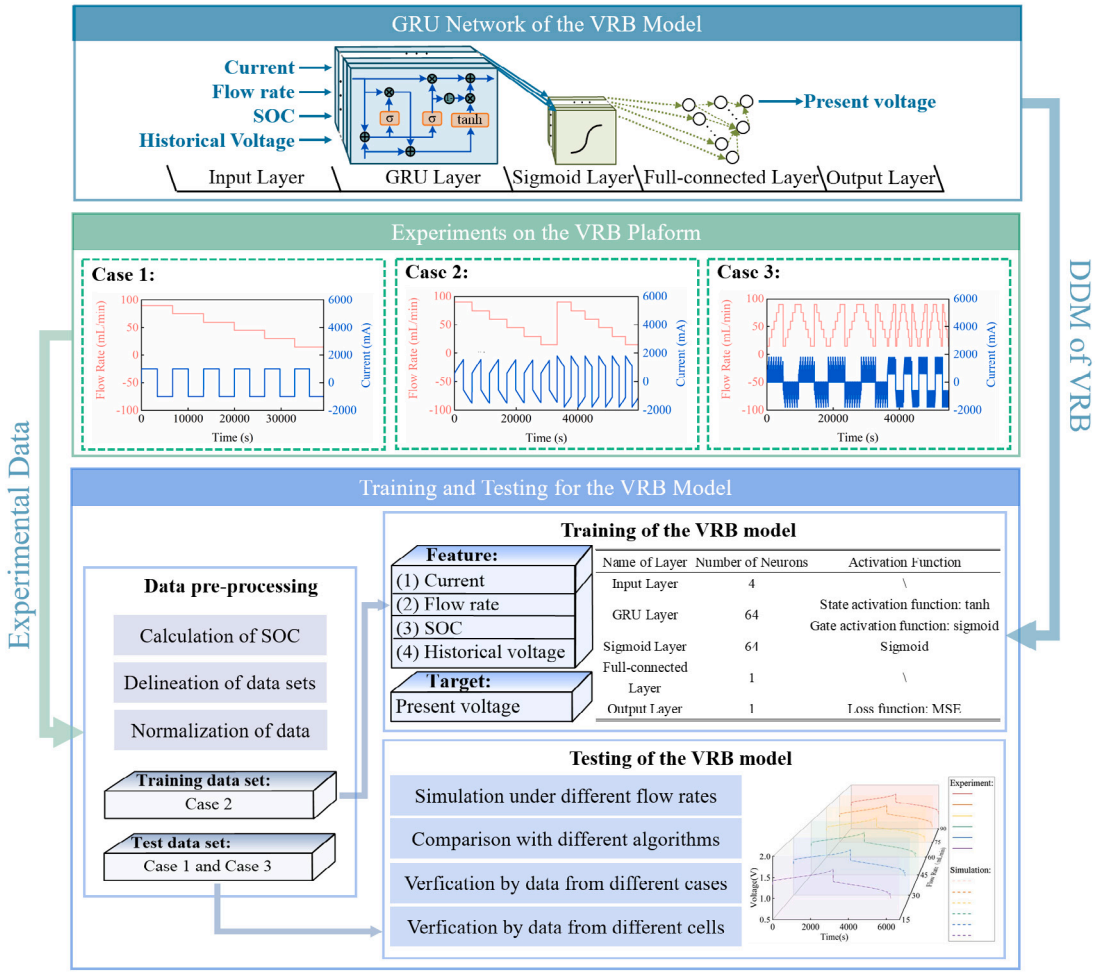

Fig. 1. Framework of the proposed flow-rate-aware DDM of VRBs.

where $\hat{y}_i$ is the predicted value of the output y_i, $f(\bar{x}_i, \theta)$ represents the GRU function, and θ represents all the parameters (W, U, and b), and n is the number of data samples in the training set. The BP algorithm is used to reduce the error by adjusting the connection weights of each layer, and the weights are obtained by gradient descent, which is optimized by the Adam method. Here, the partial derivative of the loss function for the network parameter θ is:

$$h_t(\theta) = \frac{1}{n} \sum_{(\bar{x}_i, y_i) \in \mathcal{I}_n} \frac{\partial \mathcal{L}\left(y_i, f\left(\bar{x}_i, \theta\right)\right)}{\partial \theta} \tag{7}$$

where $\mathcal{I}_n$ is the selected data set. The updated gradient g_t is defined as:

$$g_t = h_t\left(\theta_{t-1}\right) \tag{8}$$

The first-order moment M_t and second-order moment G_t of g_t are calculated by:

$$M_t = \beta_1 M_{t-1} + \left(1 - \beta_1\right) g_t \tag{9}$$

$$G_t = \beta_2 G_{t-1} + (1 - \beta_2) g_t^2 \tag{10}$$

where $\beta_1 = 0.9$ and $\beta_2 = 0.999$ are two dynamic average rates. M_t and G_t are updated to correct possible biases:

$$\hat{M}_t = \frac{M_t}{1 - \beta_1^t} \tag{11}$$

$$\hat{G}_t = \frac{G_t}{1 - \beta_2^t} \tag{12}$$

Then, the new parameters are updated according to:

$$\theta_t = \theta_{t-1} + \Delta\theta_t = \theta_{t-1} - \alpha \frac{\hat{M}_t}{\sqrt{\hat{G}_t + \varepsilon}} \tag{13}$$

Here, the parameter ε is set to 10^{-8} to ensure numerical stability during training. The initial learning rate α is set to 0.005 and after $t = 20$ s, the learning rate is multiplied by 0.2. This approach enhances the convergence and facilitates efficient adaptation of the model to the data, resulting in improved overall performance.

3. Experimental platform and data acquisition

3.1. Experimental platform setup

The proposed DDM framework underwent rigorous validation via an experimental platform, depicted in Fig. 3(a). This platform consists of three primary components: a VRB system, a battery testing system, and a host computer, all of which are provided by Wuhan Zhisheng New Energy Co., Ltd. Within the VRB system, two cells with identical materials and building structures were used, as depicted in Fig. 3(b). The specifications of the experimental platform are detailed in Table 2. This configuration facilitated comprehensive testing and analysis, ensuring the reliability and efficacy of the proposed DDM framework for VRB modeling.

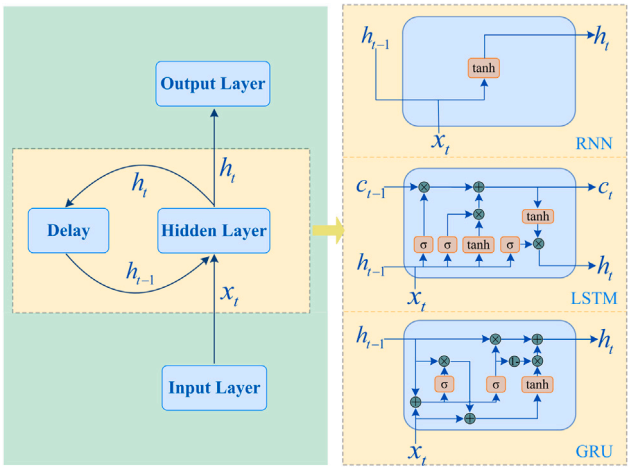

Fig. 2. RNN, LSTM, and GRU structures.

Table 2
Specification of the experimental VRB system.

Parameters	Setting
Electrolyte volume	25 mL
Electrolyte concentration	1.7 mol/L
Charge cutoff voltage	1.7 V
Discharge cutoff voltage	1.0 V
Number of cells	1
Shape of flow channels	Serpentine
Current density	200 mA/cm^2
Electrode size	3 cm × 3 cm
Membrane material	Perfluorosulfur

3.2. Experimental design

Three cases were designed by considering different currents and flow rates, as shown in Fig. 3. They are described as follows.

(1) Case 1: Constant flow rate and constant current in one cycle

To verify the impact of flow rate on the terminal voltage and to examine the ability to learn the trend under different flow rates, one-cycle experiments at a constant current of 1.0 A were conducted under different constant flow rates of 90 mL/min–15 mL/min (15 mL/min interval).

(2) Case 2: Constant flow rate and variable currents in one cycle

Experiments with constant flow rate and variable currents have been conducted at 90 mL/min- 15 mL/min (15 mL/min interval) to learn the relationship between the voltage and the flow rates and currents. Two sub-cases were examined:

(a) The current increases from 0.6 A, with a step change of 0.02 A every minute until reaching 1.8 A.

(b) The current decreases from 1.8 A, with a step change of −0.02 A every minute until reaching 0.6 A.

For example, during one specific charge–discharge cycle, the flow rate is set at a constant value of 15 mL/min, current conditions is set to sub-condition (a)

(3) Case 3: Variable flow rates and variable currents in one cycle

To further verify the adaptability of the proposed model to simultaneous variable flow rates and currents, experiments with variable flow rates and variable currents in one cycle have been conducted. The flow rate sub-conditions include:

(a) The flow rate increases stepwise. It starts at 15 mL/min and increases by 15 mL/min every 6 or 12 mins until reaching 90 mL/min.

(b) The flow rate decreases stepwise. It starts at 90 mL/min and is reduced by 15 mL/min every 6 or 12 mins until reaching 15 mL/min.

At every flow rate, the current sub-condition include:

(a) The current increases linearly. It starts at 0.6 A and increases by 0.2 A/min until reaching 1.8 A.

(b) The current decreases linearly. It starts at 1.8 A and decreases by 0.2 A/min until reaching 0.6 A.

(c) The current increases stepwise. It starts at 0.6 A and increases by 0.3 A every 3 min until reaching 1.8 A, with a duty cycle of 50%.

(d) The current decreases stepwise. It starts at 1.8 A and decreases by 0.3 A every 3 min until reaching 0.6 A, with a duty cycle of 50%.

There are two types of current sub-conditions and four types of flow rate sub-conditions, resulting in a total of eight different operating conditions. For example, during one specific charge–discharge cycle, the flow rate is set to sub-condition (a), current is set to sub-condition (a).

3.3. Data preprocessing and analysis

The measured raw data were preprocessed as follows. (a) Deletion of the pause segments. During these periods, the experiment was paused to facilitate the manual adjustment of the flow rates. Therefore, the data segments with these manual pause actions must be removed. (b) Calculation of SOC. First, the VRB capacity is calibrated by low-current experiments. The nominal charging capacity is $Q_{\text{nom,chg}}$ = 1107.175 mA h, and the discharging capacity is $Q_{\text{nom,dch}}$ = 1070.925 mA h. The SOC data can thus be calculated by:

$$\text{SOC}_{\text{chg}} = \text{SOC}_0 + \frac{Q_{\text{acc}}}{Q_{\text{nom,chg}}} \tag{14}$$

$$\text{SOC}_{\text{dch}} = \text{SOC}_{\text{chg}} - \frac{Q_{\text{acc}}}{Q_{\text{nom,dch}}} \tag{15}$$

where SOC_0 is the initial SOC, Q_{acc} is the accumulated charge calculated as the integration of battery current, and SOC_{chg} and SOC_{dch} denote the charging and discharging SOC, respectively.

The data obtained from VRB experiments are visualized in Fig. 4. It can be seen that the terminal voltage of VRB varies with flow rates, currents, and SOC. Among all features, the flow rate is unique for the VRB. The voltages under different flow rates are shown in Fig. 5, clearly indicating that substantial impact of flow rate on voltage. As the flow rate increases, both the growth rate of charging voltage in Fig. 5(a) and the reduction rate of discharging voltage in Fig. 5(b) decrease. In addition, the black contour lines in Fig. 5 show that the change rate of the terminal voltage decreases as the flow rate increases.

3.4. Performance metrics for model evaluation

The mean absolute error (MAE), root-mean-square error (RMSE), and the coefficient of determination R-square (R^2) will be used as the metrics to evaluate the model performance. They are defined by

$$\text{MAE} = \frac{1}{n}\sum_{i=1}^{n}\left|\hat{y}_i - y_i\right| \tag{16}$$

$$\text{RMSE} = \sqrt{\frac{1}{n}\sum_{i=1}^{n}\left(\hat{y}_i - y_i\right)^2} \tag{17}$$

$$\text{R}^2 = 1 - \frac{\sum_{i=1}^{n}\left(\hat{y}_i - \bar{y}_i\right)^2}{\sum_{i=1}^{n}\left(\hat{y}_i - y_i\right)^2} \tag{18}$$

where y is the actual value, $\hat{y}$ is the predicted value from the model, and $\bar{y}$ is the mean value. n is the number of data samples in the corresponding data set.

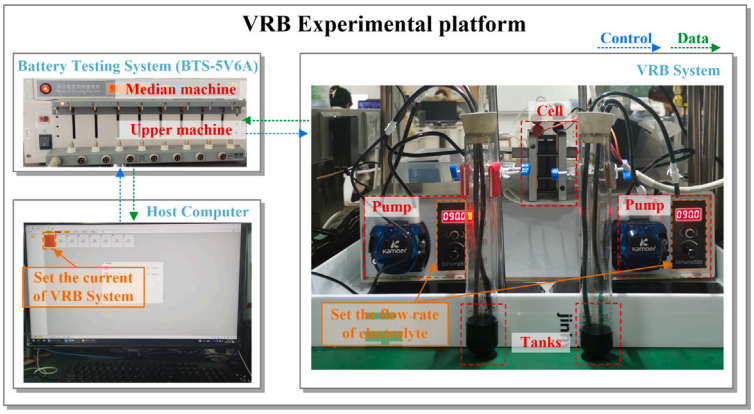

(a)

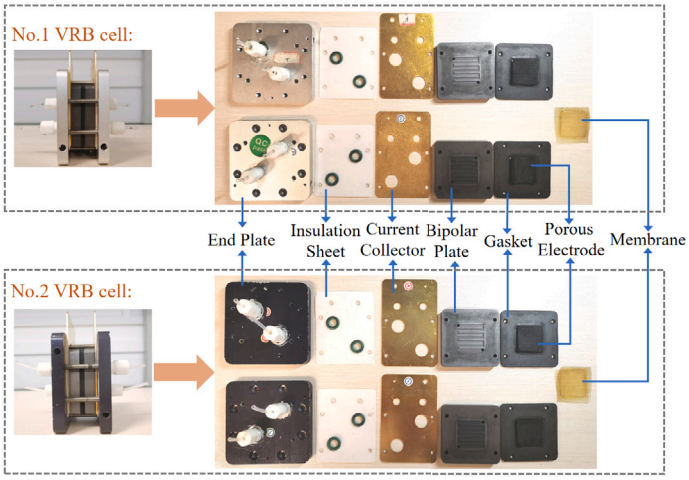

(b)

Fig. 3. VRB experimental platform: (a) Composition structure of the experimental platform; (b) Stack structures of the two cells.

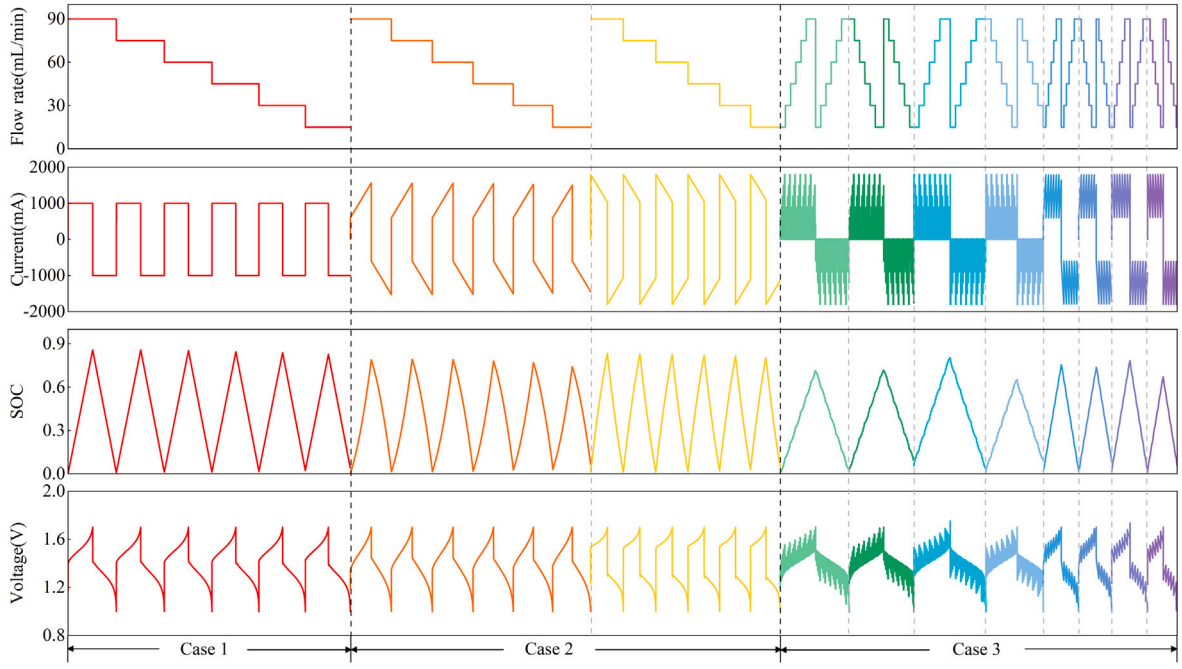

Fig. 4. Waveforms of VRB experimental data.

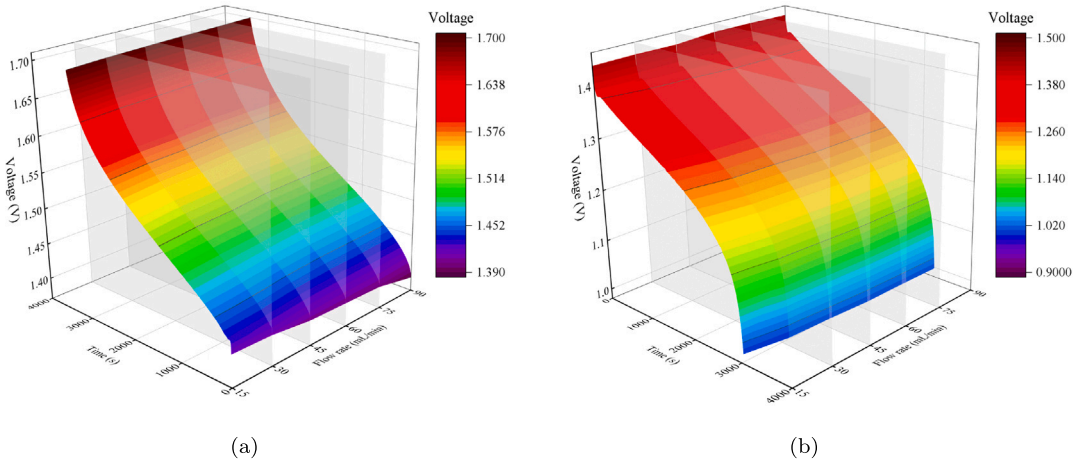

Fig. 5. Surfaces of VRB voltage as a function of flow rate and time during the (a) charging and (b) discharging processes.

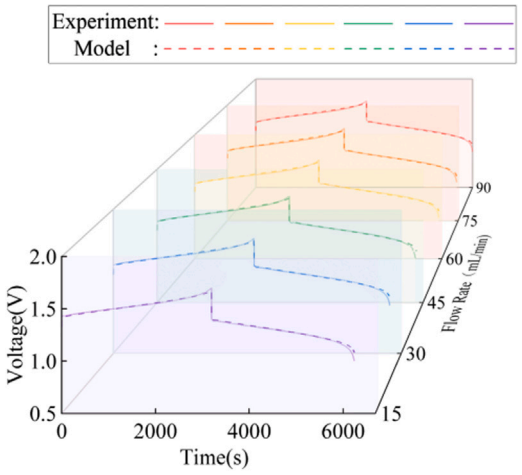

Fig. 6. Comparison between the predicted voltage and experimental results under different constant flow rates in six cycles. The same constant current is applied for different cycles.

Table 3
Performance indicators based on the results with constant flow rate and constant current in one cycle.

Flow rate (mL/min)	15	30	45	60	75	90
MAE	0.0055	0.0053	0.0052	0.0058	0.0059	0.0058
RMSE	0.0095	0.0088	0.0095	0.0090	0.0091	0.0091
R^2	0.9958	0.9962	0.9954	0.9958	0.9957	0.9957

4. Results and discussion

4.1. Model performance under different flow rates

The measured data from Case 2 served for model training, and the accuracy of different models was assessed by comparing their predictions with the measured data obtained from Cases 1 and 3. Fig. 6 presents a visual comparison between the VRB terminal voltage predicted by the GRU neural network for Case 1 and the corresponding experimental measurements, with fixed constant current but different constant flow rates applied during six cycles. The model's performance is evaluated and summarized in Table 3.

The results show that the developed GRU neural network demonstrates excellent accuracy in predicting the VRB terminal voltage across various flow rate conditions, with the MAE and RMSE consistently below 0.0059 V and 0.0095 V, respectively. These errors are as low as 0.35% and 0.56%, respectively, when compared to the maximum battery voltage of 1.7 V. In Fig. 6, both the charging and discharging processes show nearly linear voltage changes over time until reaching their respective endpoints. Throughout these periods, the GRU neural network's the predicted voltage aligns well with the actual data. To ensure safe operation, the battery's cutoff voltage was artificially set during experiments. However, the collected dataset contains limited information about the cutoff voltage, posing challenges for conventional GRU models to learn effectively. This limitation can lead to an unfavorable prediction error, potentially causing overcharging or overdischarging. To address this concern and enhance safety, our model incorporates a sigmoid layer to constrain the GRU's output within the range of $[0, 1]$. Here, 0 and 1 correspond to the maximum and minimum voltage limits after normalization, respectively. By applying this approach, the model significantly reduces the prediction error and mitigates the risk of overcharging or overdischarging during operation.

4.2. Model comparison

4.2.1. Comparison with ECMs

To examine the data processing capability of the proposed DDM at different flow rates, the DDM was compared with a VRB model based on the first-order RC equivalent circuit in Case 1. As shown in Fig. 7, for the GRU model, as demonstrated in Section 4.1, its terminal voltage adapts to different flow rates since the model captures the coupling hydrodynamic and electric behaviors buried in the training data. In contrast, the ECM relies on basic transformations and linear combinations of negative exponential functions, rendering it inadequate in reproducing the voltage segments attributed to the nonlinear dynamic behaviors of the system. In addition, the ECM neglects the impact of flow rates on external characteristics, leading to a failure to reflect variable flow rates in the predicted voltage. The GRU performance is therefore much superior to the ECM under the variable flow rate conditions.

Note that during the final stages of charging and discharging (approximately the last 20 min), significant nonlinear voltage behaviors are observed in Fig. 7. The proposed GRU model exhibits superior adaptability to the variations in internal characteristics, thanks to its remarkable ability to handle time-series data. At the end of the discharge, the maximum error is less than 0.1096 V, and the time error to reach the end of discharge is less than 1 min. In contrast, while the maximum error of the ECM is 0.1475 V, which may not seem significantly higher than the GRU model, the corresponding time error in predicting the end of discharge reaches up to 12 min.

Table 4
Comparison of performance indicators of SVM, BP, and GRU models.

Algorithm	SVM			BPNN			GRU		
	MAE	RMSE	R^2	MAE	RMSE	R^2	MAE	RMSE	R^2
15 mL/min	0.0319	0.0395	0.8935	0.0081	0.0114	0.9933	0.0056	0.0098	0.9953
30 mL/min	0.0288	0.0338	0.9272	0.0071	0.0104	0.9942	0.0053	0.0088	0.9961
45 mL/min	0.0268	0.0311	0.9407	0.0069	0.0101	0.9944	0.0052	0.0087	0.9962
60 mL/min	0.0260	0.0300	0.9446	0.0063	0.0096	0.9947	0.0058	0.0091	0.9957
75 mL/min	0.0267	0.0311	0.9382	0.0068	0.0100	0.9943	0.0059	0.0092	0.9957
90 mL/min	0.0299	0.0350	0.9165	0.0075	0.0106	0.9935	0.0058	0.0091	0.9957

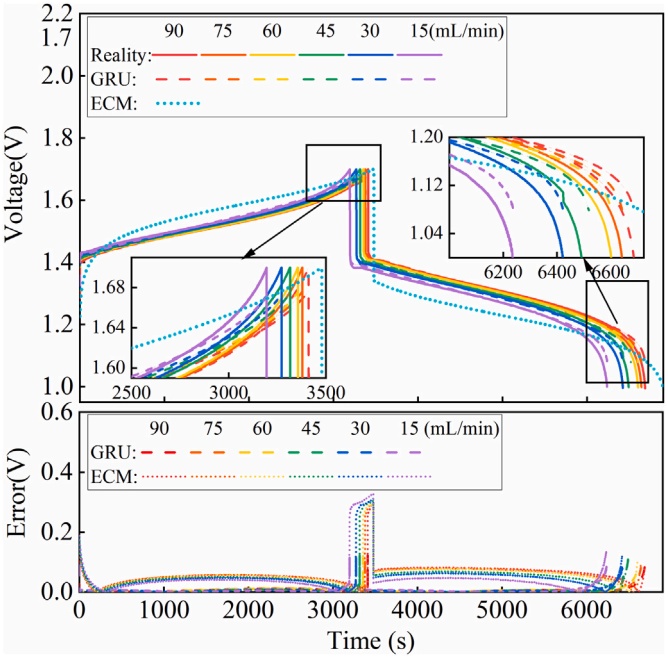

Fig. 7. Comparison of results between an ECM and the proposed GRU model.

4.2.2. Comparison with state-of-the-art DDMs

A comparison of Case 1 between the proposed GRU model with two widely adopted DDMs, SVM and BPNN, is presented in Table 4. The results clearly demonstrate that the VRB model based on GRU outperforms SVM and BPNN in terms of various evaluation indicators. Specifically, SVM demonstrates the largest error, with its accuracy showing significant fluctuations across various flow rates. Notably, SVM records its highest error at a flow rate of 15 mL/min, reaching a MAE of 0.0319 V. This is attributed to SVM's conventional nature as a machine learning algorithm, devoid of deep neural network structures. Instead, SVM relies on mathematical and geometric principles for model training and prediction, making it ill-suited for capturing the intricate dynamics of voltage fluctuations during battery operation.

In contrast, BPNN and GRU, both popular deep learning algorithms, exhibit comparable performance indicators across different flow rates. However, it is important to note that BPNN struggles to handle temporal data, learning individual data samples in isolation. On the other hand, GRU excels in processing time-series data and accurately capturing the nonlinear variations in battery terminal voltage. The MAE of GRU consistently remains below 0.0056 V, showcasing its superior predictive capabilities. Hence, GRU was chosen to build our battery model.

4.3. Model validation under different operating conditions

A VRB serves as a power source that frequently operates under changing currents, experiencing acceleration, deceleration, and pulsed current conditions when utilized for renewable energy storage. The flow rate is a vital operational parameter in flow batteries, directly impacting the oxidation–reduction reactions within the cell stack. For VRBs, a low flow rate causes an increase in concentration overpotential within the battery. This speeds up the battery's approach to the cutoff voltage and consequently reduces the efficiency. On the other hand, when the flow rate is too high, the electrolyte does not react sufficiently within the battery, leading to a drop in the operational efficiency. As such, it becomes imperative to assess the adaptability of the VRB model across various scenarios. The results from Case 3, involving linear current variation under different flow rates, are presented in Fig. 8, and the performance indicators for variable flow rates and linear currents are given in Table 5. The model showcases strong generalization capabilities and impressive temporal processing capacity. It effectively analyzes the temporal relationship between input and output vectors, enabling it to adapt dynamically to the fluctuations in VRB's internal characteristics. This capacity ensures the model's effectiveness in capturing the complexities of real-world operational conditions and enhances its ability to deliver accurate predictions for different VRB scenarios.

Table 5
Performance indicators based on the results under variable and linear currents.

Case	Linear current	Increase	Increase	Decrease	Decrease
	Pulsed flow rate	Increase	Decrease	Increase	Decrease
MAE		0.0065	0.0058	0.0079	0.0059
RMSE		0.0095	0.0090	0.0120	0.0119
R^2		0.9964	0.9965	0.9945	0.9945

The pumps used in our experiments must be stopped at the instance of switching the flow rates. Therefore, there is a shift point of the terminal voltage at the point of flow rate switching. However, the conventional model faces challenges, showing significant oscillations during the simulation of the shift point and suffering from a substantial deviation in fitting the edges. In contrast, the proposed model can successfully control the oscillation within a narrow range using the feature extractor of GRU, leading to a mean error of 0.0734 V at the shift point. This noteworthy improvement in simulation accuracy at jump points enables the model to better replicate the entire charging and discharging process, especially when dealing with variable currents.

Compared to Case 3 of linear current variation in Fig. 8, it becomes evident that the shift points of the terminal voltage appear more frequently in the case of pulsed current variation. Fig. 9 displays the results of shift points for Case 3, with step increases in flow rates and current. The distance between the predicted and actual values is effectively limited within a narrow range. The terminal voltage under pulsed current conditions undergoes five distinct jumps at every flow rate, showing the model's excellent learning ability to adapt to changes in external characteristics. The evaluating indicators for experiments featuring variable flow rates and pulsed currents in a single cycle are summarized in Table 6. The model achieves exceptional performance, with an MAE of 0.0067 V for data from experiments with step-transformation currents and the RMSEs within the range of 0 – 0.0146 V. These results highlight the model's excellent capabilities and reinforce its capacity to deliver accurate predictions in the face of dynamic conditions with pulsed currents and variable flow rates.

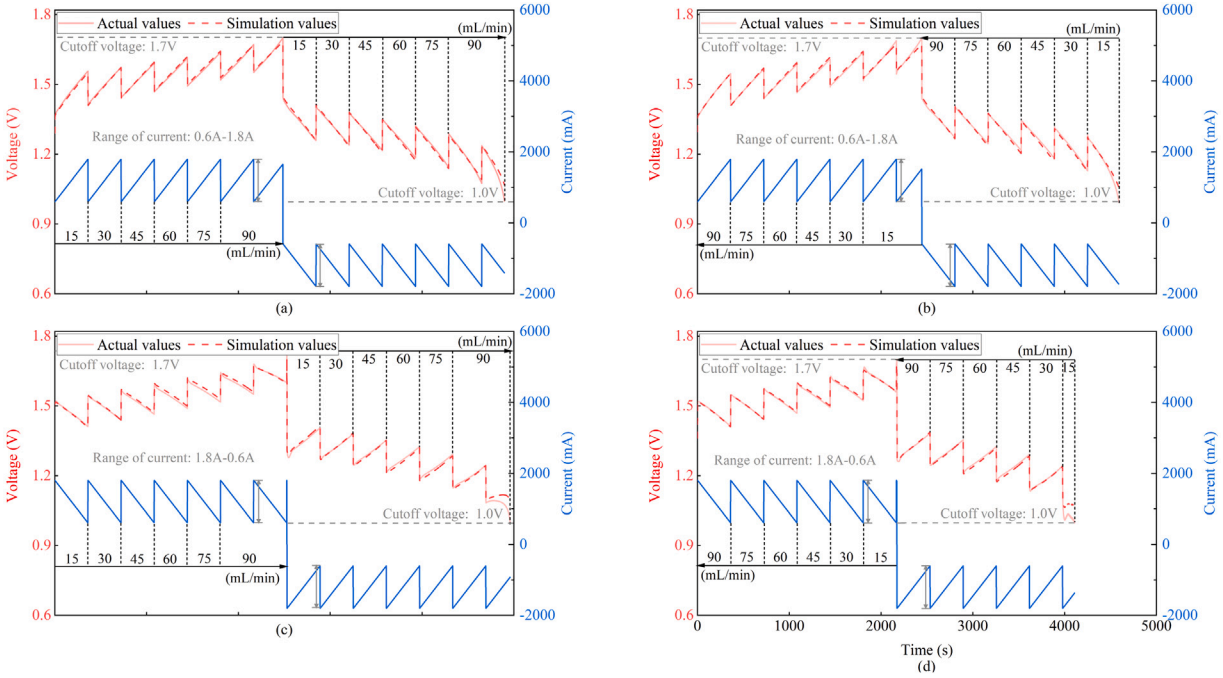

Fig. 8. Results for data with the case of the linear current variation. (a) Linear increase in current/step increase in flow rate(b) Linear increase in current/step decrease in flow rate(c) Linear decrease in current/step increase in flow rate(d) Linear decrease in current/step decrease in flow rate.

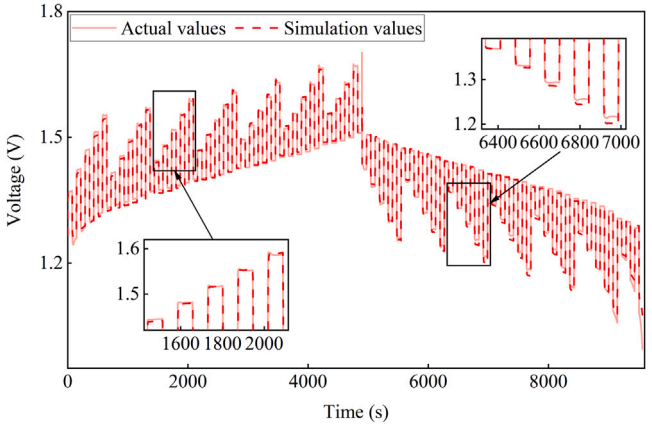

Fig. 9. Results of shift points of the case with step increase flow rate and step increase current.

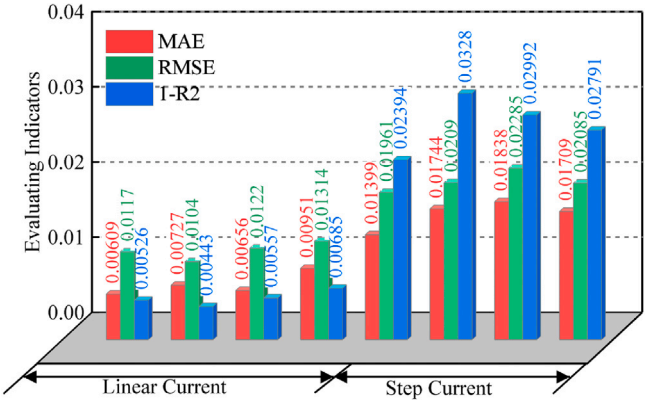

Fig. 10. Model performance metrics for results from the Cell 2.

Table 6
Performance indicators for experiments with variable flow rates and pulsed currents in one cycle.

Case	Pulsed current	Increase	Increase	Decrease	Decrease
	Pulsed flow rate	Increase	Decrease	Increase	Decrease
MAE		0.0067	0.0067	0.0080	0.0055
RMSE		0.0139	0.0134	0.0146	0.0123
R^2		0.9869	0.9864	0.9864	0.9882

4.4. Evaluation of model robustness

To demonstrate the model's robustness to different cell parameters, we conducted experiments on two VRB cells, accounting for potential cell inconsistency. The earlier Cases 1–3 were replicated for both cells. The model was trained using the data from Cell 1, and for testing, one-cycle experiment data from Cell 2 were employed as the test set, encompassing the variable flow rates and currents.

Fig. 10 illustrates the performance indicators for the results obtained from Case 3 of Cell 2. The model presents excellent prediction accuracy for data with linear current, as demonstrated by all three evaluating indicators. Notably, the model's RMSE remains well below 0.013 V for data from linear current variation experiments, indicating its precise prediction of Cell 2's terminal voltage. Furthermore, the proposed model effectively limits the RMSE within a specific range of less than 0.023 V for operating conditions involving pulsed current. This level of accuracy meets the requirement of typical VRB models for management and control purposes. Consequently, the VRB modeling method, based on the GRU neural network while considering flow rates can be extended to simulate the terminal voltage of VRB with the same type and applicable to various related applications.

5. Conclusions

This paper presents a novel data-driven modeling approach for vanadium redox flow batteries (VRB) using a gated recurrent unit

(GRU) neural network targeting variable flow rate applications. By incorporating electrolyte flow rates and considering the time-series nature and nonlinearity of VRB characteristics, the developed model enables accurate prediction of the terminal voltage at different flow rates and enhances the precision of nonlinear data analysis. The proposed GRU model takes inputs such as flow rate, current, state of charge, and voltage, all while eliminating the need to consider internal operating principles. This streamlining greatly reduces the model's complexity, making it well-suited for real-time operation. To evaluate the model's performance, simulations were conducted at different flow rates, and the results in the nonlinear section are compared with those from widely utilized equivalent circuit model. This comparison demonstrates the superior data processing capabilities of the proposed model. In addition, the effectiveness of the data-driven algorithm is assessed by comparing it with other existing methods. The proposed model is validated using experimental data from various test cases and another VRB cell of the same type. The results clearly demonstrate the modeling method's adaptability to achieve high performance prediction.

CRediT authorship contribution statement

Binyu Xiong: Conceptualization, Methodology, Writing – original draft, Resources, Supervision, Funding acquisition. **Jinrui Tang:** Methodology, Investigation, Supervision, Writing – review & editing. **Yang Li:** Methodology, Writing – review & editing, Supervision, Funding acquisition. **Peng Zhou:** Writing – review & editing, Formal analysis. **Shaofeng Zhang:** Writing – original draft, Software, Investigation, Visualization. **Xinan Zhang:** Writing – review & editing. **Chaoyu Dong:** Writing – review & editing. **Hoay Beng Gooi:** Writing – review & editing.

Declaration of competing interest

The authors declare that they have no known competing financial interests or personal relationships that could have appeared to influence the work reported in this paper.

Data availability

Data will be made available on request.

Acknowledgments

This work was supported by the National Natural Science Foundation of China under Grant #52177221.

References

[1] K. Lourenssen, J. Williams, F. Ahmadpour, R. Clemmer, S. Tasnim, Vanadium redox flow batteries: A comprehensive review, J. Energy Storage 25 (2019) 100844, http://dx.doi.org/10.1016/j.est.2019.100844.

[2] M. Guarnieri, P. Mattavelli, G. Petrone, G. Spagnuolo, Vanadium redox flow batteries: Potentials and challenges of an emerging storage technology, IEEE Ind. Electron. Mag. 10 (4) (2016) 20–31, http://dx.doi.org/10.1109/MIE.2016.2611760.

[3] J.H. Vinco, A.E.E. da Cunha Domingos, D.C.R. Espinosa, J.A.S. Tenório, M. dos Passos Galluzzi Baltazar, Unfolding the vanadium redox flow batteries: An indeep perspective on its components and current operation challenges, J. Energy Storage 43 (2021) 103180, http://dx.doi.org/10.1016/j.est.2021.103180.

[4] B.R. Chalamala, T. Soundappan, G.R. Fisher, M.R. Anstey, V.V. Viswanathan, M.L. Perry, Redox flow batteries: An engineering perspective, Proc. IEEE 102 (6) (2014) 976–999, http://dx.doi.org/10.1109/JPROC.2014.2320317.

[5] P. Alotto, M. Guarnieri, F. Moro, Redox flow batteries for the storage of renewable energy: A review, Renew. Sustain. Energy Rev. 29 (2014) 325–335, http://dx.doi.org/10.1016/j.rser.2013.08.001.

[6] C. Choi, H. Noh, S. Kim, R. Kim, J. Lee, J. Heo, H.-T. Kim, Understanding the redox reaction mechanism of vanadium electrolytes in all-vanadium redox flow batteries, J. Energy Storage 21 (2019) 321–327, http://dx.doi.org/10.1016/j.est.2018.11.002.

[7] J.-W. Ni, M.-J. Li, T. Ma, W. Wei, Z. Li, The configuration optimized design method based on real-time efficiency for the application of vanadium redox flow battery in microgrid, Energy Conv. Manag. 267 (2022) 115899, http://dx.doi.org/10.1016/j.enconman.2022.115899.

[8] L. Briot, M. Petit, Q. Cacciuttolo, M.-C. Pera, Aging phenomena and their modelling in aqueous organic redox flow batteries: A review, J. Power Sources 536 (2022) 231427, http://dx.doi.org/10.1016/j.jpowsour.2022.231427.

[9] V. Di Noto, K. Vezzù, G. Crivellaro, G. Pagot, C. Sun, L. Meda, I.A. Rutkowska, P.J. Kulesza, T.A. Zawodzinski, A general electrochemical formalism for vanadium redox flow batteries, Electrochim. Acta 408 (2022) 139937, http://dx.doi.org/10.1016/j.electacta.2022.139937.

[10] B. Xiong, Y. Li, Y. Ding, J. Zhao, Z. Wei, X. Ai, J. Fang, Numerical analysis of vanadium redox flow batteries considering electrode deformation under various flow fields, J. Power Sources 564 (2023) 232814, http://dx.doi.org/10.1016/j.jpowsour.2023.232814.

[11] Y. Zhang, J. Zhao, P. Wang, M. Skyllas-Kazacos, B. Xiong, R. Badrinarayanan, A comprehensive equivalent circuit model of all-vanadium redox flow battery for power system analysis, J. Power Sources 290 (2015) 14–24, http://dx.doi.org/10.1016/j.jpowsour.2015.04.169.

[12] B. Xiong, Y. Yang, J. Tang, Y. Li, Z. Wei, Y. Su, Q. Zhang, An enhanced equivalent circuit model of vanadium redox flow battery energy storage systems considering thermal effects, IEEE Access 7 (2019) 162297–162308, http://dx.doi.org/10.1109/ACCESS.2019.2952212.

[13] X. Binyu, Z. Jiyun, L. Jinbin, Modeling of an all-vanadium redox flow battery and optimization of flow rates, in: 2013 IEEE Power & Energy Society General Meeting, 2013, pp. 1–5, http://dx.doi.org/10.1109/PESMG.2013.6672599.

[14] M.H. Li, T. Funaki, T. Hikihara, A study of output terminal voltage modeling for redox flow battery based on charge and discharge experiments, in: 2007 Power Conversion Conference - Nagoya, 2007, pp. 221–225, http://dx.doi.org/10.1109/PCCON.2007.372971.

[15] A. Bhattacharjee, H. Samanta, N. Banerjee, H. Saha, Development and validation of a real time flow control integrated mppt charger for solar PV applications of vanadium redox flow battery, Energy Conv. Manag 171 (2018) 1449–1462, http://dx.doi.org/10.1016/j.enconman.2018.06.088.

[16] A. Khazaeli, A. Vatani, N. Tahouni, M.H. Panjeshahi, Numerical investigation and thermodynamic analysis of the effect of electrolyte flow rate on performance of all vanadium redox flow batteries, J. Power Sources 293 (2015) 599–612, http://dx.doi.org/10.1016/j.jpowsour.2015.05.100.

[17] Z. Huang, A. Mu, L. Wu, H. Wang, Vanadium redox flow batteries: Flow field design and flow rate optimization, J. Energy Storage 45 (2022) 103526, http://dx.doi.org/10.1016/j.est.2021.103526.

[18] Y. Zhang, R. Xiong, H. He, M.G. Pecht, Long short-term memory recurrent neural network for remaining useful life prediction of lithium-ion batteries, IEEE Trans. Veh. Technol. 67 (7) (2018) 5695–5705, http://dx.doi.org/10.1109/TVT.2018.2805189.

[19] B. Xiao, Y. Liu, B. Xiao, Accurate state-of-charge estimation approach for lithium-ion batteries by gated recurrent unit with ensemble optimizer, IEEE Access 7 (2019) 54192–54202, http://dx.doi.org/10.1109/ACCESS.2019.2913078.

[20] Q. He, Y. Fu, P. Stinis, A. Tartakovsky, Enhanced physics-constrained deep neural networks for modeling vanadium redox flow battery, J. Power Sources 542 (2022) 231807, http://dx.doi.org/10.1016/j.jpowsour.2022.231807.

[21] X. Mao, S. Song, F. Ding, Optimal BP neural network algorithm for state of charge estimation of lithium-ion battery using PSO with levy flight, J. Energy Storage 49 (2022) 104139, http://dx.doi.org/10.1016/j.est.2022.104139.

[22] G. Zhang, B. Xia, J. Wang, Intelligent state of charge estimation of lithium-ion batteries based on L-M optimized back-propagation neural network, J. Energy Storage 44 (2021) 103442, http://dx.doi.org/10.1016/j.est.2021.103442.

[23] E. Chemali, P.J. Kollmeyer, M. Preindl, A. Emadi, State-of-charge estimation of li-ion batteries using deep neural networks: A machine learning approach, J. Power Sources 400 (2018) 242–255, http://dx.doi.org/10.1016/j.jpowsour.2018.06.104.

[24] S. König, M.R. Suriyah, T. Leibfried, Volumetric electrolyte flow rate control in vanadium redox flow batteries using a variable flow factor, in: IREC2015 the Sixth International Renewable Energy Congress, 2015, pp. 1–6, http://dx.doi.org/10.1109/IREC.2015.7110861.

[25] Z. Xi, R. Wang, Y. Fu, C. Mi, Accurate and reliable state of charge estimation of lithium ion batteries using time-delayed recurrent neural networks through the identification of overexcited neurons, Appl. Energy 305 (2022) 117962, http://dx.doi.org/10.1016/j.apenergy.2021.117962.

[26] X. Feng, J. Chen, Z. Zhang, S. Miao, Q. Zhu, State-of-charge estimation of lithium-ion battery based on clockwork recurrent neural network, Energy 236 (2021) 121360, http://dx.doi.org/10.1016/j.energy.2021.121360.

[27] Y. Liu, R. Li, B. Xiong, S. Zhang, X. Zhang, H. Iu, T. Fernando, A novel vanadium redox flow battery modelling method using honey badger optimization assisted CNN-BiLSTM, J. Power Sources 558 (2023) 232610, http://dx.doi.org/10.1016/j.jpowsour.2022.232610.

[28] Q. He, P. Stinis, A.M. Tartakovsky, Physics-constrained deep neural network method for estimating parameters in a redox flow battery, J. Power Sources 528 (2022) 231147, http://dx.doi.org/10.1016/j.jpowsour.2022.231147.

[29] A.A. Howard, T. Yu, W. Wang, A.M. Tartakovsky, Physics-informed CoKriging model of a redox flow battery, J. Power Sources 542 (2022) 231668, http://dx.doi.org/10.1016/j.jpowsour.2022.231668.

[30] R. Zhao, P.J. Kollmeyer, R.D. Lorenz, T.M. Jahns, A compact unified methodology via a recurrent neural network for accurate modeling of lithium-ion battery voltage and state-of-charge, in: 2017 IEEE Energy Conversion Congress and Exposition, ECCE, 2017, pp. 5234–5241, http://dx.doi.org/10.1109/ECCE.2017.8096879.

[31] R.K. Sankaralingam, S. Seshadri, J. Sunarso, A.I. Bhatt, A. Kapoor, Overview of the factors affecting the performance of vanadium redox flow batteries, J. Energy Storage 41 (2021) 102857, http://dx.doi.org/10.1016/j.est.2021.102857.

[32] B. Xiong, J. Tang, Y. Li, Z. Wang, C. Xie, X. Zhang, H.B. Gooi, Design of a two-stage control strategy of vanadium redox flow battery energy storage systems for grid application, IEEE Trans. Sustain. Energy 13 (4) (2022) 2079–2091, http://dx.doi.org/10.1109/TSTE.2022.3181751.

[33] S. Tong, J.H. Lacap, J.W. Park, Battery state of charge estimation using a load-classifying neural network, J. Energy Storage 7 (2016) 236–243, http://dx.doi.org/10.1016/j.est.2016.07.002.